Low-Valence $Zn^{\delta+}$ ($0<\delta<2$) Single-Atom Material as Highly Efficient Electrocatalyst for CO_2 Reduction

Simin Li, Siqi Zhao, Xiuyuan Lu, Marcel Ceccato, Xin-Ming Hu*, Alberto Roldan, Jacopo Catalano, Min Liu*, Troels Skrydstrup and Kim Daasbjerg*

[a] S. Li, S. Zhao, Dr. M. Ceccato, Prof. T. Skrydstrup
Carbon Dioxide Activation Center (CADIAC),
Interdisciplinary Nanoscience Center (iNANO), and Department of Chemistry
Aarhus University
Gustav Wieds Vej 14, 8000 Aarhus C, Denmark
[b] X. Lu, Assoc. Prof. A. Roldan
Cardiff Catalysis Institute, School of Chemistry
Cardiff University
Main Building, Park Place, Cardiff, CF10 3AT, UK
[c] Prof. X.-M. Hu
Environment Research Institute
Shandong University
Binhai Road 72, Qingdao 266237, China
E-mail: huxm@sdu.edu.cn
[d] Asst. Prof. J. Catalano
Department of Biological and Chemical Engineering,
Aarhus University
Åbogade 40, 8200 Aarhus N, Denmark
[e] Prof. M. Liu
State Key Laboratory of Powder Metallurgy
School of Physical and Electronics
Central South University
Changsha 410083, China
E-mail: minliu@csu.edu.cn
[f] Prof. K. Daasbjerg
Department of Chemistry and Interdisciplinary Nanoscience Center (iNANO)
Aarhus University
Langelandsgade 140, 8000 Aarhus C, Denmark
E-mail: kdaa@chem.au.dk

Supporting information for this article is given via a link at the end of the document.

Abstract: Electrochemical CO_2 reduction represents a promising approach to sustainably produce carbon-based chemicals and fuels but has been experiencing challenges in developing low-cost and efficient electrocatalysts. Herein, a nitrogen-stabilized single-atom catalyst containing low-valence zinc atoms ($Zn^{\delta+}$–NC) is reported. It is revealed that $Zn^{\delta+}$–NC contains a mixture of saturated four-coordinate ($Zn–N_4$) and unsaturated three-coordinate ($Zn–N_3$) sites. The latter makes Zn a low-valence state, as deduced from X-ray photoelectron spectroscopy, X-ray absorption fine structure spectroscopy, electron paramagnetic resonance, and density functional theory (DFT) simulation. As a result, $Zn^{\delta+}$–NC catalyzes electrochemical reduction of CO_2 to CO with near-unity selectivity in water at an overpotential as low as 310 mV. Importantly, a record-high current density up to 1 A cm^{-2} can be achieved together with high CO selectivity of >95% using $Zn^{\delta+}$–NC in a flow cell reactor. DFT calculations suggest that the unsaturated $Zn–N_3$ site could dramatically reduce the energy barrier by stabilizing the COOH* (* represents active sites) intermediate due to the electron-rich environment of Zn. This work sheds light on not only the relationship between coordination number, valence state, and catalytic performance of Zn single-atom sites, but it also succeeds in achieving high current densities relevant for industrial applications.

Introduction

The electrochemical CO_2 reduction reaction (eCO_2RR) represents a promising solution for mitigation of excessive CO_2 concentration in the atmosphere as well as for utilization and transformation of CO_2 into value-added chemicals and commodities.[1] This technology, if powered by renewable energy such as solar and wind power, has great potential to reach industrial level and achieve long-term energy storage.[2] Nonetheless, the inert nature of the CO_2 molecule impedes its direct electrochemical conversion, requiring large overpotential to overcome the high activation barrier. Even worse, the hydrogen evolution reaction (HER) is kinetically more favorable and will unavoidably compete with eCO_2RR under aqueous conditions. This results in low energy utilization and poor selectivity toward the target products. In general, activity is also severely limited by low solubility and slow diffusion of CO_2 in aqueous media. Thus, it is of paramount importance to improve the scalability of eCO_2RR by designing affordable catalysts that overcome the challenges regarding activity and selectivity.[3]

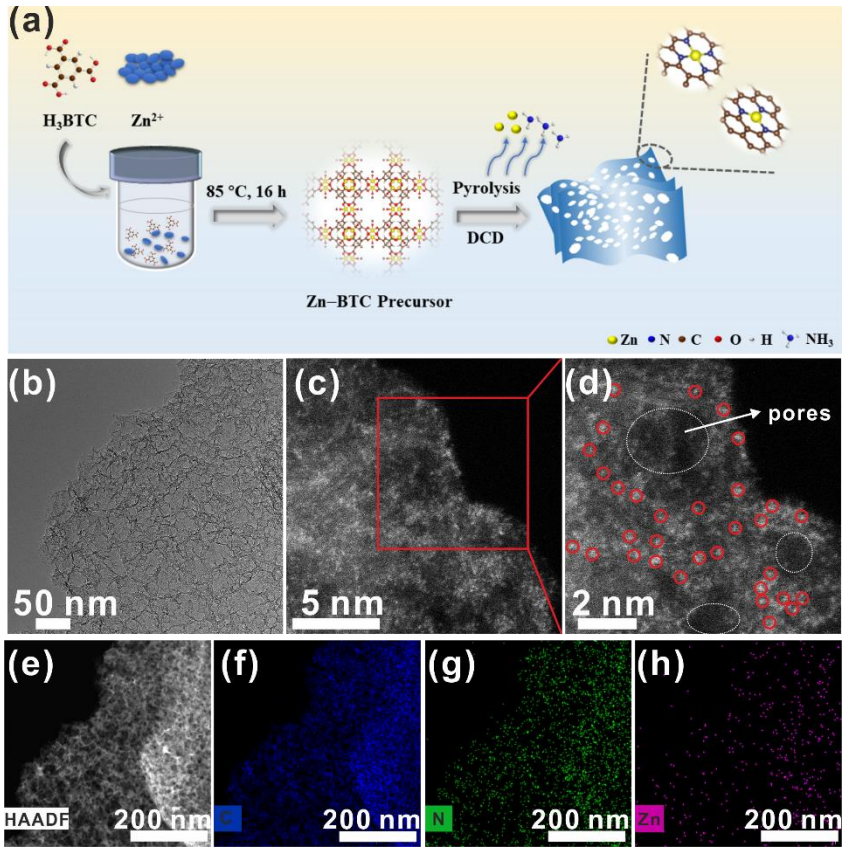

Figure 1. (a) Fabrication protocol of $Zn^{\delta+}$–NC along with (b) TEM, (c,d) aberration-corrected HAADF-STEM, and (e–h) STEM images with corresponding elemental mapping.

To date, metal-nitrogen co-decorated carbon (M–NC) materials, featured with atomically dispersed metal cations, are emerging heterogeneous catalysts. M–NC materials have the possibility of achieving maximal utilization of metal atoms and good performance in electrocatalysis due to the unique electronic properties of the isolated metal sites.[4] Among a variety of M–NC catalysts (e.g. Ni–NC, Fe–NC, and Co–NC),[5] Zn–NC has experienced little progress for two reasons. First, Zn has both low melting (692 K) and boiling (1180 K) points, making it difficult to incorporate it into the carbon structure, as it readily evaporates during pyrolysis.[6] In fact, Zn-containing precursors are often used to fabricate metal-free porous carbon materials, exploiting the removal of Zn under heat treatment.[7] Second, unlike other earth-abundant transition metals (i.e. Fe, Co, Ni, and Cu), which have unfilled 3d orbitals with facilitated charge transfer as their characteristic feature, the fully occupied $3d^{10}$ configuration of Zn severely impedes electron movement and diminishes its electrocatalytic activity. The nature of the active site in catalysts comprising isolated Zn atoms is intensely debated. For some Zn-based complexes, the active sites have been suggested to be the ligands or adjacent carbon atoms, instead of the Zn (II) center which is considered to be inactive for electrocatalysis.[8] In contrast, other studies have shown that Zn-based single-atom catalysts (SACs) can be responsible for CO_2 conversion.[9] For instance, Zhu et al. studied the coexistence of Zn and Co single atoms on N-doped carbon and put forward evidence that electronic interaction between Zn and Co atoms facilitated COOH* formation on the former to boost CO production in eCO_2RR (to 93%).[10] Fang et al. and Hao et al. addressed the curvature of $Zn–N_x$ sites as a way to improve eCO_2RR by increasing the electron density of the Zn 3d orbital.[11] Although these studies showed significant improvement in eCO_2RR, further development would still be required to make industrial applications of Zn-based SACs viable. Great challenges still remain; how to construct highly efficient catalyst versions of this type, and how to gain fundamental mechanic understanding of the exact nature of active sites.

Herein, we report a nitrogen-stabilized low-valence Zn-based SAC ($Zn^{\delta+}$–NC) prepared by pyrolyzing a Zn-containing precursor in the presence of nitrogen source. On the basis of various experimental techniques, we demonstrate that the $Zn^{\delta+}$–NC catalyst contains a mixture of saturated four-coordinate $Zn–N_4$ and unsaturated three-coordinate $Zn–N_3$ sites. The latter kind of sites, which are electron-rich, lowers the oxidation state of Zn. Density functional theory (DFT) calculations corroborate that the 3d orbitals of the unsaturated $Zn–N_3$ sites are involved in binding the COOH* intermediate to effectively reduce the energy barrier of its formation. In contrast, the 3d orbital of $Zn–N_4$ is inert during eCO_2RR. Overall, this catalyst exhibits near 100% CO selectivity at a small overpotential (310 mV). Notably, $Zn^{\delta+}$–NC achieves a record-high current density of 1 A cm^{-2} when used in a flow cell electrolyzer, showing great prospect for industrial applications.

Results and Discussion

Material synthesis and characterization

$Zn^{\delta+}$–NC electrocatalysts were prepared through consecutive coordination and carbonization processes (**Figure 1a**). The Zn-containing precursor, i.e. Zn–BTC (BTC denotes benzene-1,3,5-tricarboxylic acid) was synthesized following a solvothermal method.[12] Powder X-ray diffraction (XRD) pattern confirms its good crystallinity, and scanning electron microscopy (SEM) images show a smooth slab structure of Zn–BTC, with a surface area of 23 $m^2\ g^{-1}$ determined by the Brunauer-Emmett-Teller (BET) method (**Figure S1**). Next, Zn–BTC was pyrolyzed at 1000 °C under Ar atmosphere in the presence of dicyandiamide (DCD) to produce the target material, $Zn^{\delta+}$–NC. Here, DCD serves as nitrogen source to anchor Zn single atoms through Zn–N coordination. This is accomplished as judged from the 1.08 wt% Zn content determined by inductively coupled plasma-optical emission spectroscopy (ICP-OES). SEM images of $Zn^{\delta+}$–NC show that pyrolysis leaves the surface less smooth with numerous holes exposed **(Figure S2)**. The coarse structure of $Zn^{\delta+}$–NC with coexistence of both micropores and mesopores gives it a high surface area of 332 $m^2\ g^{-1}$ and good CO_2 adsorption capacity of 34 $cm^3\ g^{-1}$ (**Figures S3** and **S4**).

Transmission electron microscopy (TEM) and high-angle annular dark-field scanning transmission electron microscopy (HAADF-STEM) images reveal that $Zn^{\delta+}$–NC possesses thin nanosheets morphology with large population of through-plane pores (**Figures 1b,e** and **S5**). Importantly, we observe neither Zn nanoparticles nor clusters across the entire structure of $Zn^{\delta+}$–NC. Instead, we see nicely distributed bright spots, corresponding to Zn atoms, from aberration-corrected HAADF-STEM (**Figure 1c,d**). Moreover, atomization of Zn after pyrolysis could be substantiated by the XRD pattern, showing only diffraction from graphitic carbon (2θ = 26° and 43°) and no Zn-based crystalline phases (**Figure S6**).[6a] Finally, elemental mapping by energy-dispersive X-ray spectroscopy reveals uniform distribution of C, N, and Zn (**Figure 1f–h)** which, together with the aberration-corrected HAADF-STEM and XRD pattern, confirms the existence of Zn single atoms in $Zn^{\delta+}$–NC.

For comparative purpose, we synthesized two control samples leaving out either the Zn or N source from the pyrolysis step. In the former case, N-doped carbon (denoted NC) was obtained (**Figures S7–S9**). In the latter case, somewhat surprisingly, the produced material contained no Zn, but only carbon (denoted BTC–C). This substantiates the indispensable role of DCD in preparation of Zn single atoms, serving to prevent Zn evaporation at high temperature by anchoring the atoms.[13] In addition, a third control sample (DP–ZnNC) was produced by pyrolyzing directly the mixture of zinc nitrate and H_3BTC to verify the importance of using the Zn–BTC framework as precursor in the Zn SAC preparation (**Figure S10**).

Valence state and fine structure of Zn

XPS was employed to characterize chemical composition and elemental state of $Zn^{\delta+}$–NC, using Zn (II) tetraphenylporphine (ZnTPP) containing Zn^{2+} and an intact Zn–N_4 core structure as reference sample (**Figure S11**). The binding energy of Zn $2p_{3/2}$ in $Zn^{\delta+}$–NC is located at 1021.6 eV, which is slightly lower than that of ZnTPP (1021.9 eV) (**Figures 2a** and **S12**).[11a] This would suggest a low-valence Zn (<2+) in $Zn^{\delta+}$–NC. In addition, Zn Auger LMM kinetic energy spectra reveal a distinct Zn LMM peak (990.0 eV) of $Zn^{\delta+}$–NC located between that of ZnTPP (987.8 eV) and Zn metal (992.0 eV) (**Figure 2b**). This corroborates the low valence state of $Zn^{\delta+}$, suggesting that a certain fraction of Zn (II) atoms have been reduced to Zn (I) during heat treatment because of the strong reductive capacity of NH_3 released from DCD.[14] The N 1s XPS spectrum of $Zn^{\delta+}$–NC (**Figure 2c)** can be deconvoluted into five types of N, including pyridinic N, Zn–N, pyrrolic N, graphitic N, and oxidized N. The presence of Zn–N species, which is further shown in N K-edge soft X-ray absorption near-edge structures (XANES) (**Figure S13a)**, supports the atomic dispersion of Zn.

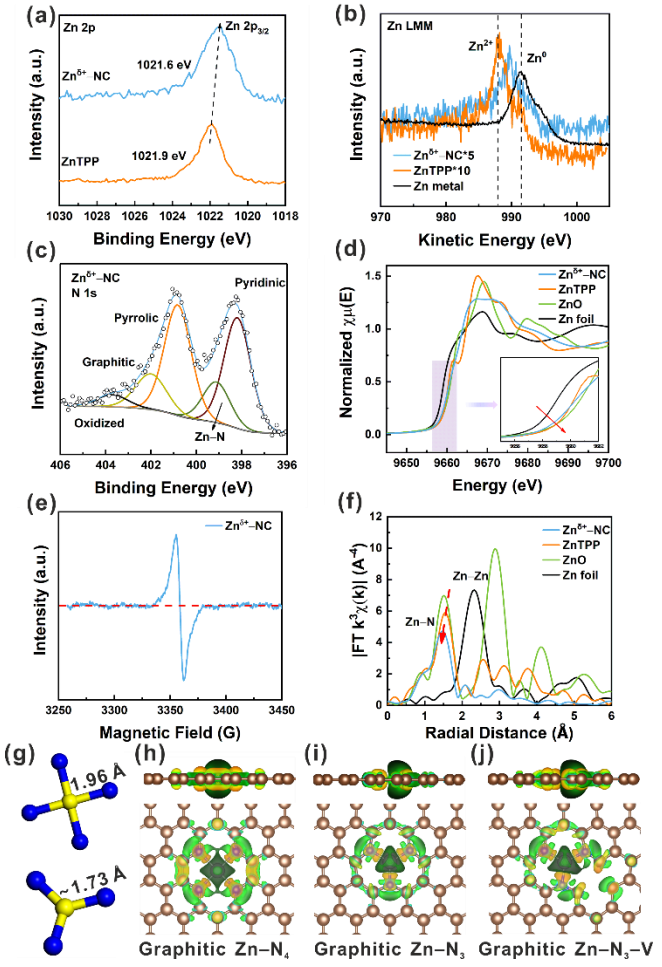

Figure 2. (a) XPS Zn 2p spectra, (b) Zn Auger LMM kinetic energy spectra, (c) N 1s spectrum, (d) Zn K-edge XANES (inset shows enlarged near-edge pattern), (e) EPR spectrum, and (f) Fourier transform of EXAFS spectra of $Zn^{\delta+}$–NC. (g) Interatomic distance between Zn center (yellow) and surrounding N atoms (blue) in graphitic Zn–N_4, Zn–N_3 (or Zn–N_3–V where V denotes vacancy) model simulated from DFT calculations. (h–j) Calculated spatial distribution of charge density for graphitic Zn–N_4, Zn–N_3, and Zn–N_3–V (yellow and green iso-surfaces denote depletion and gain of electron density, respectively, with an iso-surface value of 0.003 e $Å^{-3}$; brown color represents C atoms).

To elucidate the fine electronic structure of $Zn^{\delta+}$–NC, the Zn K-edge spectrum from XANES was analyzed with ZnTPP, ZnO, and Zn foil serving as references (**Figures 2d** and **S14**). Notably, the adsorption edge position of $Zn^{\delta+}$–NC is far away from that of Zn foil but also at somewhat lower energy than that of ZnTPP. Second, the white line intensity of $Zn^{\delta+}$–NC lies in between Zn foil

and ZnTPP/ZnO. Third, the typical D_{4h} symmetry fingerprint peak of Zn–N_4 at 9661.8 eV, as seen in the ZnTPP spectrum, disappears in $Zn^{\delta+}$–NC, indicative of a non-centrosymmetric Zn–N configuration.[15] In addition, electron paramagnetic resonance (EPR) spectroscopy shows a distinct signal (**Figure 2e**), which is attributed to the unpaired electron of Zn (I) in $Zn^{\delta+}$–NC,[8c,15] as the coordinately saturated Zn (II) would be EPR silent.[8c] All these observations point toward low valency of $Zn^{\delta+}$ ($0<\delta<2$) in $Zn^{\delta+}$–NC.

Figure 2f compares phase-uncorrected Fourier transformed (FT) EXAFS spectra of $Zn^{\delta+}$–NC, ZnTPP, ZnO, and Zn foil. In the radial distribution function from k^3-weight Zn K-edge EXAFS, no Zn–Zn bonding at 2.32 Å is detected in $Zn^{\delta+}$–NC. This excludes presence of metallic Zn in $Zn^{\delta+}$–NC and underlines good atom dispersion of Zn sites. Furthermore, because Zn–C and Zn–O bonds are excluded from C and O K-edge XANES spectra (**Figure S13b,c**) and C and O 1s XPS spectra (**Figure S15**), the first-shell main peaks at 1.47 and 1.55 Å for $Zn^{\delta+}$–NC and ZnTPP, respectively, are attributed to Zn–N coordination. The slightly shorter Zn–N interatomic distance of $Zn^{\delta+}$–NC, relative to that of ZnTPP, unveils a contracted Zn–N–C local center in $Zn^{\delta+}$–NC. Moreover, the fact that $Zn^{\delta+}$–NC displays lower peak intensity than that of the four N-coordination (Zn–N_4) in ZnTPP, suggests that the coordination number is lower than four. Taking together, XANES and EXAFS spectra consistently suggest the existence of non-centrosymmetric and unsaturated Zn–N centers in $Zn^{\delta+}$–NC.

We conducted EXAFS fitting using ZnTPP as Zn–N_4 core structure to identify the local structure of $Zn^{\delta+}$–NC (**Figure S16**). **Table S2** summarizes the fitting parameters. Notably, the average coordination number of Zn–N in $Zn^{\delta+}$–NC after first-shell fitting is 3.47, which is far less than four. It should be noted that the fitting result becomes less satisfactory using Zn–N_3 as model (with vacancy nearby or not), as evidenced from the larger *R*-factor (percentage misfit) and unmatched coordination number. These results would suggest that $Zn^{\delta+}$–NC consists of a mixture of Zn–N_4 and Zn–N_3. Furthermore, Zn–N_4, Zn–N_3, and Zn–N_3–V (V denotes vacancy) were modelled up in the graphene plane to simulate the active site structure in the viewpoint of DFT (**Figure 2g**); presence of vacancies was considered due to the observation of pores in $Zn^{\delta+}$–NC (**Figure 1**). The DFT optimized Zn–N bond distance of ~1.73 Å in both Zn–N_3 and Zn–N_3–V, is shorter than that of Zn–N_4 (1.96 Å), matching well with the radial distance in EXAFS results and fitting analysis.

Next, we employed Bader charge analysis to characterize the Zn–surface interaction using the above models (**Figure 2h–j**). Green and yellow regions refer to electron accumulation and depletion, respectively. The Zn atom possesses 10.82, 11.00, and 10.90 valence electrons after combining with N atoms in Zn–N_4, Zn–N_3, and Zn–N_3–V, respectively. Thus, the Zn atom in Zn–N_3 or Zn–N_3–V possesses an electron-richer environment compared to that in Zn–N_4, leading to lower valence state in $Zn^{\delta+}$–NC. Thus, together with the structural characterization of XAS and XPS, these results reveal the relationship between coordination number and valence state. $Zn^{\delta+}$–NC consists of a mixture of Zn(II)–N_4 and Zn(I)–N_3 sites, leading to a mix-coordinated and low-average-valence Zn–N_x ($3 \le x \le 4$) structure. Meanwhile, the Zn–N_3 and/or Zn–N_3–V could hold enough delocalized electrons to facilitate electron transfer and affect the intermediate adsorption/desorption steps during eCO_2RR.[15]

eCO_2RR performance in H-cell

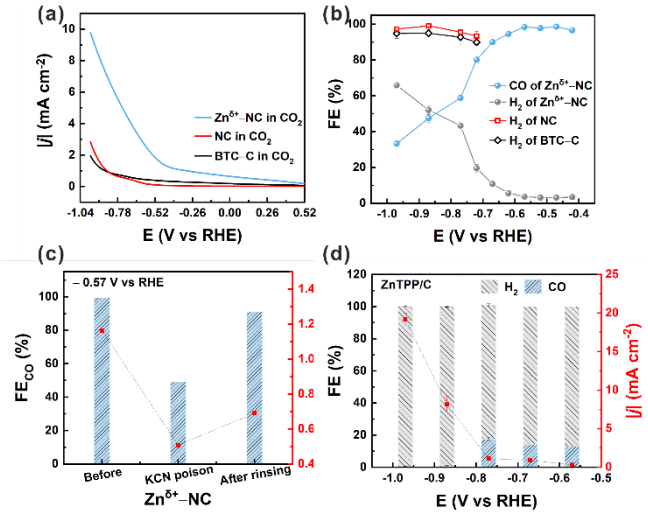

Figure 3. (a) Linear sweep voltammograms at sweep rate = 10 mV s^{-1} and (b) FE of H_2 and CO measured after 15 min electrolysis at various potentials for $Zn^{\delta+}$–NC, NC, and BTC–C. (c) FE_{CO} and $|j|$ recorded at –0.57 V vs RHE for $Zn^{\delta+}$–NC in the absence and presence of 25 mM KCN (as well as after rinsing) after 15 min electrolysis. (d) FE and $|j|$ measured at various potentials for ZnTPP/C after 15 min electrolysis. Electrolyte is CO_2-saturated 0.5 M $KHCO_3$.

To test electrocatalytic properties of the as-prepared $Zn^{\delta+}$–NC, NC, and BTC–C, linear sweep voltammograms were recorded under both CO_2 and Ar atmosphere in 0.5 M $KHCO_3$ (**Figures 3a** and **S17**). Increase of the absolute cathodic current density, $|j|$, recorded on $Zn^{\delta+}$–NC is evident upon purging CO_2 into the catholyte. Moreover, it is comparatively larger than that for the NC and BTC–C materials under the same conditions, implying that $Zn^{\delta+}$–NC exhibits much better catalytic performance for eCO_2RR.

Next, eCO_2RR activity and selectivity of the materials were evaluated in an H-cell at selected potentials between –0.97 and –0.42 V vs the reversible hydrogen electrode (RHE). CO and H_2 are the only products detected (**Figure S18**). **Figure 3b** shows that $Zn^{\delta+}$–NC gives the largest CO selectivity in the entire potential range, presenting a maximum CO faradaic efficiency (FE_{CO}) as high as 99% at –0.47 V vs RHE. However, DP–ZnNC produced via direct pyrolysis of the precursors performs significantly poorer, emphasizing the importance of the Zn–BTC template for obtaining a highly active Zn-based SAC (**Figure S19**).

Moreover, CO formation on $Zn^{\delta+}$–NC starts already at –0.42 V vs RHE, corresponding to a fairly low overpotential of 310 mV, given that the equilibrium potential for CO_2 to CO is –0.11 V vs RHE. In contrast, NC and BTC–C are both inactive for CO_2 reduction, with only H_2 being detected during electrolysis. Notably, $Zn^{\delta+}$–NC exhibits much higher $|j|$ and, in particular, $|j_{CO}|$ compared with NC and BTC–C (**Figure S20**), underlining the catalytic activity of Zn-based active sites in eCO_2RR. To a minor extent only, this enhancement can be attributed to a higher electrochemical active surface area (ECSA) of $Zn^{\delta+}$–NC, evaluated from the double-layer capacity (C_{dl}) of all electrodes (**Figure S21**). In this manner, C_{dl}, which is proportional to ECSA, was found to be 19.4, 1.9 and 9.7 mF cm^{-2} for $Zn^{\delta+}$–NC, NC, and BTC–C, respectively.

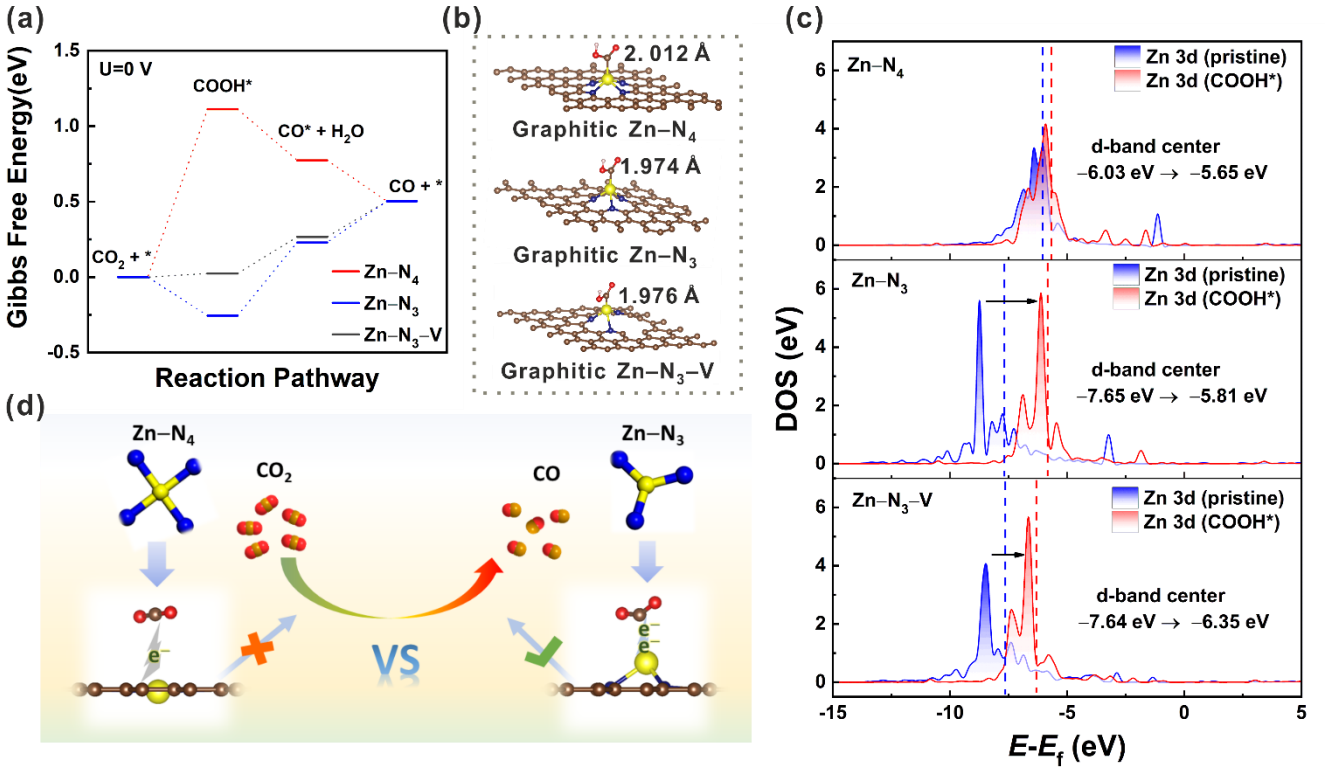

Figure 4. (a) Calculated Gibbs energy diagram for CO_2-to-CO conversion using graphitic Zn–N_4, Zn–N_3 and Zn–N_3–V models at U = 0 V and pH = 0**.** (b) DFT calculated geometry of graphitic Zn–N_4, Zn–N_3 and Zn–N_3–V sites with key intermediate COOH*-adsorbed species. (c) Projected electron density of states (DOS) of the Zn–N_4, Zn–N_3, and Zn–N_3–V models before and after COOH* interaction. (d) Comparison of the active site of electron-rich Zn–N_3 with that of Zn–N_4. Note that Zn, N, C, O, and H atoms are represented by yellow, blue, brown, red, and pink colors, respectively.

To gain deeper insight into the outstanding performance of $Zn^{\delta+}$–NC, poisoning experiments involving cyanide ions (blocking Zn atoms to suppress its reaction with CO_2) were carried out in the H-cell setup. **Figure 3c** shows that both FE_{CO} and $|j|$ display distinct decreases once CN^- is introduced to the electrolyte. After removing CN^- by washing in Milli-Q water, the activity of $Zn^{\delta+}$–NC is partially recovered, validating that isolated Zn atoms are the active sites for eCO_2RR. It is also interesting to compare the catalytic performance of $Zn^{\delta+}$–NC with that of a composite material comprising ZnTPP supported on carbon black (ZnTPP/C) (**Figures 3d, S22,** and **S23**). As seen, such Zn–N_4-containing supported catalyst with Zn oxidation state of 2+ exhibits high HER activity and produces much less CO. On this basis, we propose that the superior CO selectivity of $Zn^{\delta+}$–NC should be ascribed to its coordinatively unsaturated configuration, resulting in a distorted charge distribution (*vide infra*).

Finally, long-term stability of $Zn^{\delta+}$–NC was examined by carrying out continuous CO_2 reduction at –0.57 V vs RHE for 12 h (**Figure S24**). Encouragingly, both FE_{CO} (≈ 95.3%) and $|j|$ (≈ 0.9 mA cm^{-2}) remain stable over the entire period. XPS spectra, TEM, and elemental mapping of post-electrolysis $Zn^{\delta+}$–NC give evidence of negligible changes to the Zn oxidation state, coordination characteristics, porous structure, and distribution of active sites (**Figures S25** and **S26**). These results validate the superior durability and stability of single-atom Zn sites for eCO_2RR.

Origin of electrocatalytic activity

The EXAFS fitting results suggested that Zn–N_4 and Zn–N_3/Zn–N_3–V sites would be the central structures to consider in $Zn^{\delta+}$–NC. Thus, these three Zn–N coordinated models were used to simulate the active site structures for eCO_2RR by means of DFT calculations. In general, the reaction pathway for the CO_2-to-CO conversion is a two-electron/two-proton transfer process, in which generation of key intermediates such as COOH* and CO* (* represents active sites) is recognized as the important steps affecting eCO_2RR performance. We calculated the relative energy of the key intermediates at Zn–N_4, Zn–N_3, and Zn–N_3–V sites. **Figures 4a** and **S27** show that formation of COOH* (CO_2* + e^- + H^+ → COOH*) at Zn–N_4 is highly endothermic and becomes the rate-limiting step in eCO_2RR while the same process is less demanding on Zn–N_3 or Zn–N_3–V. Even if the specifically applied potential and electrolyte pH were to be taken into account in the calculations, the formation of COOH* would become thermodynamically even more favorable on the unsaturated Zn–N_3 and Zn–N_3–V sites than on Zn–N_4 (**Figure S28a**). In comparison, the competing HER becomes more energy-demanding, leading to sluggish kinetics of H_2 evolution on these sites (**Figure S28b**).

Furthermore, the crucial intermediate COOH* (**Figure 4b**) has Zn–C bond length on Zn–N_4, Zn–N_3 and Zn–N_3–V of 2.012, 1.974, and 1.976 Å, respectively. The decrease in Zn–C bond length with the Zn coordination indicates the strength of interaction and charge transfer between Zn atoms and COOH*. It verifies that unsaturated Zn–N_3 and/or Zn–N_3–V sites effectively smooth the pathway toward COOH* formation. Focusing on the whole energy

pathway on Zn–N_3 and/or Zn–N_3–V, the narrow energy gap between each step indicates less energy requests to trigger eCO_2RR, which could therefore explain the experimentally observed low overpotential of 310 mV. Besides, we found from Bader charge distribution (**Figure 2h–j**) that unsaturated Zn sites hold more electrons. Thus, we ascribe the low free energy of COOH* formation to the electron-rich environment, which enhances electron movement to accelerate the COOH* step and through this boost overall eCO_2RR.

Up to this point, we systemically identified the unsaturated Zn–N_3 (and/or Zn–N_3–V) active sites for eCO_2RR. To understand the inactivity of Zn–N_4 sites, we introduced projected electron density of states (DOS) analysis to investigate the electronic interaction between the Zn center and the COOH* intermediate (**Figures 4c** and **S29**). Comparison of the Zn 3d orbital in the pristine Zn–N_4, Zn–N_3, and Zn–N_3–V models before and after interacting with COOH* reveals that the change of the d-band center of Zn 3d in Zn–N_4 is negligible. In contrast, it shows upshift in both Zn–N_3 and Zn–N_3–V, corresponding to electron transfer from Zn to the adsorbate. These results imply that there is almost no electron movement from the Zn 3d orbitals of Zn–N_4 to the antibonding orbitals of *COOH, thus being inert toward eCO_2RR. This is also consistent with results reported elsewhere that the 3d orbital of Zn (II) is resistant to participate in catalytic reactions due to the fulfilled electron configuration.[8b,8c,15] Conversely, accompanying the large upshift of the d-band center of Zn–N_3 and Zn–N_3–V, more electrons in the 3d orbital participate in stabilizing COOH* to promote eCO_2RR in these cases. Thus, it is the coordinately unsaturated Zn sites in $Zn^{\delta+}$–NC that effectively accelerate electron movement and prompt the catalytic activity, playing a main active role throughout the whole process (**Figure 4d**).

eCO_2RR performance in flow cell–toward industrial applications

To assess the potential of the $Zn^{\delta+}$–NC catalyst for industrial applications, we fabricated a custom-designed flow cell (**Figures S30 and S31a**) to scale up eCO_2RR to industrially relevant current densities (>100 mA cm^{-2}).[16] First, we assembled the $Zn^{\delta+}$–NC catalyst on a gas diffusion electrode (GDE) with mass loading of 1 mg cm^{-2}. Unlike the H-cell, where the catalysis occurs in a two-phase interphase (electrode/electrolyte), the flow cell configuration creates a three-phase interface of CO_2 (gas), protons (liquid), and catalyst (solid). Notably, CO_2 is directly fed to the cathode in the gas phase to overcome the issue of inherently low mass transport of CO_2 reagents in aqueous media.[17] In addition, highly alkaline electrolyte (1 M KOH) was employed to suppress the competing HER during eCO_2RR.

Remarkably, FE_{CO} remains at 95 ± 4% while increasing $|j|$ from 0.2 to 1.0 A cm^{-2} (**Figures 5a** and **S31b**). In addition, the Zn 2p XPS spectrum of $Zn^{\delta+}$–NC after electrolysis at 1 A cm^{-2} (**Figure S32)** shows that the Zn oxidation state is left unchanged under these conditions, indicating superior stability of low-valence Zn sites. The turnover frequency of $Zn^{\delta+}$–NC catalyst in flow cell is more than hundred times higher than that in the H-cell, reaching over 1.1×10^5 h^{-1} at $|j|$ = 1.0 A cm^{-2} on the assumption that all Zn sites participate in the reaction (**Figure S33**). In addition, a longer-term galvanostatic test performed at $|j|$ = 0.5 A cm^{-2} with $Zn^{\delta+}$–NC for 1.5 h shows stable WE potential with FE_{CO} > 90%. In other words, the $Zn^{\delta+}$–NC catalyst exhibits excellent performance in terms of both CO production and current density, thus showing the superiority of the gas-fed configuration compared with the H-cell setup. After 1.5 h, cell stability issues become evident with the WE potential becoming more negative and FE_{CO} experiencing severe decrease (**Figure 5b**). Furthermore, if $|j|$ is enhanced beyond 1 A cm^{-2}, severe flooding of the GDE happens, resulting in large fluctuations in WE potential and sharp decay of FE_{CO} from 99% to 32% within the first hour (**Figure S34**). Such lack of durability at high operating current density is fully consistent with literature,[18] and it shows that further optimization would be requested of both the GDE and cell configuration to expand the operational time window.[19] This being said, the successful demonstration of a flow-cell setup for $Zn^{\delta+}$–NC with $|j|$ = 1 A cm^{-2} is an important first step toward scaling of eCO_2RR. In fact, the performance reported herein is superior when compared with recently reported SACs applied in the GDE reactor (**Figure 5c, Table S3**). In conclusion, the record-large $|j|$ = 1 A cm^{-2}, together with high FE_{CO} > 95% for CO_2-to-CO conversion, provides great prospect for industrial applications.

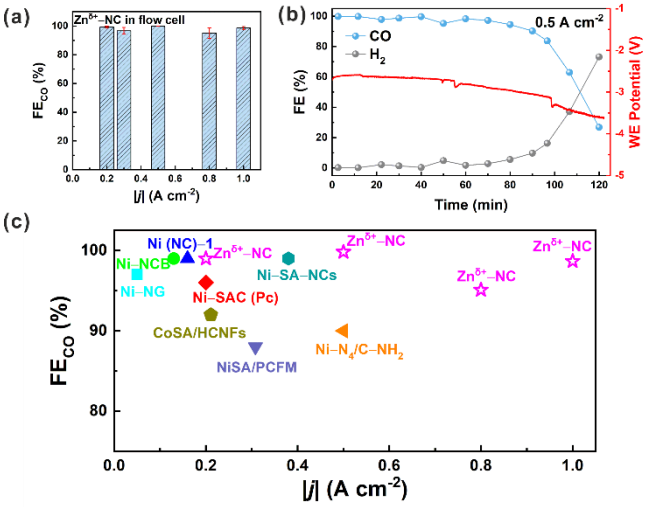

Figure 5. Recording of FE on $Zn^{\delta+}$–NC with (a) $|j|$ varying from 0.2–1.0 A cm^{-2} for 10 min electrolysis and with (b) $|j|$ = 0.5 A cm^{-2} for 2 h electrolysis of CO_2 using a gas-fed flow-cell reactor (not *iR*-corrected) in 1 M KOH. (c) Comparison of FE_{CO} and $|j|$ for state-of-the-art SACs using flow or membrane electrode assembly cells (**Table S3**).

Conclusion

We successfully synthesized a nitrogen-anchored low-valence Zn-based SAC ($Zn^{\delta+}$–NC) showing excellent performance for electrochemical CO_2-to-CO conversion in aqueous medium. Comprehensive characterizations of $Zn^{\delta+}$–NC consistently reveals the specific fine structure of Zn single atoms, consisting of both Zn–N_4 and Zn–N_3 sites. The latter structure (or with a vacancy, i.e., Zn–N_3–V) holds enough electrons to reduce the average valence of Zn in $Zn^{\delta+}$–NC (i.e., less than 2+). DFT calculations disclose that the main effect of the partial unsaturated Zn–N_3 (and/or Zn–N_3–V) sites is to lower the energy reaction pathway for forming the crucial COOH* intermediate. Importantly, the mix-coordinated Zn SACs display excellent selectivity for CO production (~99%) at a fairly small overpotential (310 mV) during electrochemical CO_2 reduction. From an industrial perspective,

the $Zn^{\delta+}$–NC catalyst achieves a remarkable current density of 1 A cm^{-2} with high CO selectivity using a flow cell reactor. Overall, this work reveals the relationship between coordination number, valence state, and catalytic performance, serving as guidelines for designing and developing atomically dispersed active sites for electrocatalytic CO_2 reduction at industrially relevant activity.

Acknowledgements

We thank the Danish National Research Foundation (grant no. DNRF118) and research grant from VILLUM FONDEN (grant no. 36196) for generous financial support. Simin Li (CSC no. 201806370200), Siqi Zhao (CSC no. 201906920080) and Xiuyuan Lu (CSC No. 201806370221) acknowledge the China Scholarship Council. Via membership of the UK's HPC Materials Chemistry Consortium, which is funded by EPSRC (EP/L000202, EP/R029431, EP/T022213), this work used the UK Materials and Molecular Modelling Hub for computational resources, MMM Hub, which is partially funded by EPSRC (EP/T022213/1). We also acknowledge computing time on the facilities at Cardiff University managed by the Advanced Research Computing @ Cardiff (ARCCA). X.-M. Hu acknowledges the support of Qilu Young Scholars program from Shandong University and Taishan Scholars program from Shandong Province. M. Liu thanks the Natural Science Foundation of China (grant no. 21872174 and U1932148), International Science and Technology Cooperation Program (grant no. 2017YFE0127800 and 2018YFE0203402), Hunan Province Key Field R&D Program (2020WK2002), Hunan Provincial Natural Science Foundation (2020JJ2041 and 2020JJ5691). We are grateful to Dr. Ying-Rui Lu, Dr. Ting-Shan Chan at TLS 01C1 and TLS 16A1 beamlines of the National Synchrotron Radiation Research Center (NSRRC) for help with characterizations and PhD Kang Liu for fruitful discussions on XAFS results.

Conflict of interest

The authors declare no conflict of interest.

Keywords: CO_2 reduction • zinc single atoms• electrocatalysis at scale • low valence • coordination environment

References

[1] M. B. Ross, P. De Luna, Y. Li, C.-T. Dinh, D. Kim, P. Yang, E. H. Sargent, *Nat. Catal.* **2019**, *2*, 648–658.

[2] L. Fan, C. Xia, F. Yang, J. Wang, H. Wang, Y. Lu, *Sci. Adv.* **2020**, *6*, eaay3111.

[3] W. Ju, A. Bagger, G.-P. Hao, A. S. Varela, I. Sinev, V. Bon, B. Roldan Cuenya, S. Kaskel, J. Rossmeisl, P. Strasser, *Nat. Commun.* **2017**, *8*, 944.

[4] a) A. Wang, J. Li, T. Zhang, *Nat. Rev. Chem.* **2018**, *2*, 65–81; b) H. Zhang, G. Liu, L. Shi, J. Ye, *Adv. Energy Mater.* **2018**, *8*, 1701343; c) C. Cai, M. Wang, S. Han, Q. Wang, Q. Zhang, Y. Zhu, X. Yang, D. Wu, X. Zu, G. E. Sterbinsky, Z. Feng, M. Gu, *ACS Catal.* **2021**, *11*, 123–130.

[5] a) K. Jiang, S. Siahrostami, T. Zheng, Y. Hu, S. Hwang, E. Stavitski, Y. Peng, J. Dynes, M. Gangisetty, D. Su, K. Attenkofer, H. Wang, *Energy Environ. Sci.* **2018**, *11*, 893–903; b) F. Pan, B. Li, E. Sarnello, Y. Fei, X. Feng, Y. Gang, X. Xiang, L. Fang, T. Li, Y. H. Hu, G. Wang, Y. Li, *ACS Catal.* **2020**, *10*, 10803–10811; c) Y. Pan, R. Lin, Y. Chen, S. Liu, W. Zhu, X. Cao, W. Chen, K. Wu, W.-C. Cheong, Y. Wang, *J. Am. Chem. Soc.* **2018**, *140*, 4218–4221; d) X.-M. Hu, H. H. Hval, E. T. Bjerglund, K. J. Dalgaard, M. R. Madsen, M.-M. Pohl, E. Welter, P. Lamagni, K. B. Buhl, M. Bremholm, M. Beller, S. U. Pedersen, T. Skrydstrup, K. Daasbjerg, *ACS Catal.* **2018**, *8*, 6255–6264; e) S. Li, M. Ceccato, X. Lu, S. Frank, N. Lock, A. Roldan, X.-M. Hu, T. Skrydstrup, K. Daasbjerg, *J. Mater. Chem. A* **2021**, *9*, 1583–1592.

[6] a) Y. Zhang, L. Jiao, W. Yang, C. Xie, H. L. Jiang, *Angew. Chem. Int. Ed.* **2021**, *60*, 7607–7611; b) Q. Wang, T. Ina, W.-T. Chen, L. Shang, F. Sun, S. Wei, D. Sun-Waterhouse, S. G. Telfer, T. Zhang, G. I. N. Waterhouse, *Sci. Bull.* **2020**, *65*, 1743–1751.

[7] a) F. Li, Y. Bu, G.-F. Han, H.-J. Noh, S.-J. Kim, I. Ahmad, Y. Lu, P. Zhang, H. Y. Jeong, Z. Fu, *Nat. Commun.* **2019**, *10*, 1–7; b) C. Zhao, X. Dai, T. Yao, W. Chen, X. Wang, J. Wang, J. Yang, S. Wei, Y. Wu, Y. Li, *J. Am. Chem. Soc.* **2017**, *139*, 8078–8081; c) J. Gu, C.-S. Hsu, L. Bai, H. M. Chen, X. Hu, *Science* **2019**, *364*, 1091–1094; d) J. Wu, H. Zhou, Q. Li, M. Chen, J. Wan, N. Zhang, L. Xiong, S. Li, B. Y. Xia, G. Feng, *Adv. Energy Mater.* **2019**, *9*, 1900149.

[8] a) Y. Wu, J. Jiang, Z. Weng, M. Wang, D. L. J. Broere, Y. Zhong, G. W. Brudvig, Z. Feng, H. Wang, *ACS Cent. Sci.* **2017**, *3*, 847–852; b) X. Jiang, H. Li, J. Xiao, D. Gao, R. Si, F. Yang, Y. Li, G. Wang, X. Bao, *Nano Energy* **2018**, *52*, 345–350; c) S. Dou, J. Song, S. Xi, Y. Du, J. Wang, Z. F. Huang, Z. J. Xu, X. Wang, *Angew. Chem. Int. Ed.* **2019**, *58*, 4041–4045; d) L. Ye, Y. Ying, D. Sun, Z. Zhang, L. Fei, Z. Wen, J. Qiao, H. Huang, *Angew. Chem. Int. Ed.* **2020**, *132*, 3270–3277.

[9] a) F. Yang, P. Song, X. Liu, B. Mei, W. Xing, Z. Jiang, L. Gu, W. Xu, *Angew. Chem. Int. Ed.* **2018**, *57*, 12303–12307; b) Q. Yang, C. C. Yang, C. H. Lin, H. L. Jiang, *Angew. Chem. Int. Ed.* **2019**, *58*, 3511–3515.

[10] W. Zhu, L. Zhang, S. Liu, A. Li, X. Yuan, C. Hu, G. Zhang, W. Deng, K. Zang, J. Luo, Y. Zhu, M. Gu, Z. J. Zhao, J. Gong, *Angew. Chem. Int. Ed.* **2020**, *59*, 12664–12668.

[11] a) M. Fang, X. Wang, X. Li, Y. Zhu, G. Xiao, J. Feng, X. Jiang, K. Lv, Y. Zhu, W. F. Lin, *ChemCatChem* **2021**, *13*, 603–609; b) Z. Hao, J. Chen, D. Zhang, L. Zheng, Y. Li, Z. Yin, G. He, L. Jiao, Z. Wen, X.-J. Lv, *Sci. Bull.* **2021**, https://doi.org/10.1016/j.scib.2021.04.020.

[12] M. K. Bhunia, J. T. Hughes, J. C. Fettinger, A. Navrotsky, *Langmuir* **2013**, *29*, 8140–-8145.

[13] E. Zhang, T. Wang, K. Yu, J. Liu, W. Chen, A. Li, H. Rong, R. Lin, S. Ji, X. Zheng, Y. Wang, L. Zheng, C. Chen, D. Wang, J. Zhang, Y. Li, *J. Am. Chem. Soc.* **2019**, *141*, 16569–16573.

[14] a) Z. Chen, K. Mou, S. Yao, L. Liu, *ChemSusChem* **2018**, *11*, 2944–2952; b) H. Wu, H. Li, X. Zhao, Q. Liu, J. Wang, J. Xiao, S. Xie, R. Si, F. Yang, S. Miao, X. Guo, G. Wang, X. Bao, *Energy Environ. Sci.* **2016**, *9*, 3736–3745.

[15] J. Wang, H. Li, S. Liu, Y. Hu, J. Zhang, M. Xia, Y. Hou, J. Tse, J. Zhang, Y. Zhao, *Angew. Chem. Int. Ed.* **2021**, *133*, 183–187.

[16] a) H.-Y. Jeong, M. Balamurugan, V. S. K. Choutipalli, E.-S. Jeong, V. Subramanian, U. Sim, K. T. Nam, *J. Mater. Chem. A* **2019**, *7*, 10651–10661; b) H. Yang, Q. Lin, C. Zhang, X. Yu, Z. Cheng, G. Li, Q. Hu, X. Ren, Q. Zhang, J. Liu, C. He, *Nat. Commun.* **2020**, *11*, 593.

[17] a) Z. Chen, X. Zhang, W. Liu, M. Jiao, K. Mou, X. Zhang, L. Liu, *Energy Environ. Sci.* **2021**, *14*, 2349–2356; b) Y. Wang, Z. Jiang, X. Zhang, Z. Niu, Q. Zhou, X. Wang, H. Li, Z. Lin, H. Zheng, Y. Liang, *ACS Appl. Mater. Interfaces* **2020**, *12*, 33795–33802; c) T. Zheng, K. Jiang, N. Ta, Y. Hu, J. Zeng, J. Liu, H. Wang, *Joule* **2019**, *3*, 265–278.

[18] X. Zhang, Y. Wang, M. Gu, M. Wang, Z. Zhang, W. Pan, Z. Jiang, H. Zheng, M. Lucero, H. Wang, G. E. Sterbinsky, Q. Ma, Y.-G. Wang, Z. Feng, J. Li, H. Dai, Y. Liang, *Nat. Energy* **2020**, *5*, 684–692.

[19] F. P. García de Arquer, C.-T. Dinh, A. Ozden, J. Wicks, C. McCallum, A. R. Kirmani, D.-H. Nam, C. Gabardo, A. Seifitokaldani, X. Wang, Y. C. Li, F. Li, J. Edwards, L. J. Richter, S. J. Thorpe, D. Sinton, E. H. Sargent, *Science* **2020**, *367*, 661–666.

Graphical Abstract

Nitrogen-anchored low-valence Zn single-atom catalyst, containing coordinately unsaturated $Zn–N_3$ active sites, can boost electrochemical CO_2 reduction to industrial application level.